THE UNIVERSITY of EDINBURGH

Edinburgh Research Explorer

Microscopic Quantum Transport Processes of Out-of-Plane Charge Flow in 2D Semiconductors Analyzed by a Fowler–Nordheim Tunneling Probe

Citation for published version:
Shin, DH, Lee, DH, Choi, SJ, Kim, S, Kim, H, Watanabe, K, Taniguchi, T, Campbell, EEB, Lee, SW & Jung, S 2023, 'Microscopic Quantum Transport Processes of Out-of-Plane Charge Flow in 2D Semiconductors Analyzed by a Fowler–Nordheim Tunneling Probe', *Advanced Electronic Materials*, vol. 9, no. 6, 2300051. https://doi.org/10.1002/aelm.202300051

Digital Object Identifier (DOI):
10.1002/aelm.202300051

Link:
Link to publication record in Edinburgh Research Explorer

Document Version:
Publisher's PDF, also known as Version of record

Published In:
Advanced Electronic Materials

General rights
Copyright for the publications made accessible via the Edinburgh Research Explorer is retained by the author(s) and / or other copyright owners and it is a condition of accessing these publications that users recognise and abide by the legal requirements associated with these rights.

Take down policy
The University of Edinburgh has made every reasonable effort to ensure that Edinburgh Research Explorer content complies with UK legislation. If you believe that the public display of this file breaches copyright please contact openaccess@ed.ac.uk providing details, and we will remove access to the work immediately and investigate your claim.

Download date: 30. Jul. 2023

Check for updates

ADVANCED ELECTRONIC MATERIALS
Open Access
www.advelectronicmat.de

Microscopic Quantum Transport Processes of Out-of-Plane Charge Flow in 2D Semiconductors Analyzed by a Fowler–Nordheim Tunneling Probe

Dong Hoon Shin, Duk Hyun Lee, Sang-Jun Choi, Seonyeong Kim, Hakseong Kim, Kenji Watanabe, Takashi Taniguchi, Eleanor E. B. Campbell, Sang Wook Lee, and Suyong Jung**

Weak interlayer couplings at 2D van der Waals (vdW) interfaces fundamentally distinguish out-of-plane charge flow, the information carrier in vdW-assembled vertical electronic and optical devices, from the in-plane band transport processes. Here, the out-of-plane charge transport behavior in 2D vdW semiconducting transition metal dichalcogenides (SCTMD) is reported. The measurements demonstrate that, in the high electric field regime, especially at low temperatures, either electron or hole carrier Fowler–Nordheim (FN) tunneling becomes the dominant quantum transport process in ultrathin SCTMDs, down to monolayers. For few-layer SCTMDs, sequential layer-by-layer FN tunneling is observed to dominate the charge flow, thus serving as a material characterization probe for addressing the Fermi level positions and the layer numbers of the SCTMD films. Furthermore, it is shown that the physical confinement of the electron or hole carrier wave packets inside the sub-nm thick semiconducting layers reduces the vertical quantum tunneling probability, leading to an enhanced effective mass of tunneling carriers.

1. Introduction

Van der Waals (vdW) vertical heterostructures with assorted 2D materials have drawn much attention for upcoming low-dimensional electronic and optical device applications thanks to unlimited combinatorial choices for assembling heterostacks and engineering diverse functionalities.[1–5] Atomically clean vdW interfaces with negligible chemical and electrostatic interlayer bonding make expectations of novel high-performance devices realistically achievable.[1,6] In particular, 2D materials with a sizable energy gap of 1 eV or more; for example, MoS_2, WSe_2, and *h*BN, have been implemented as high-quality tunnel barriers or as efficient charge-blocking layers in various device applications such as resonant tunnel diodes,[7,8] transistor,[9–11] logic devices,[4,12] memories,[10,13,14] light-emitting diodes,[15,16] and photodetectors.[5,17,18]

D. H. Shin,[+] E. E. B. Campbell, S. W. Lee
Department of Physics
Ewha Womans University
Seoul 03760, Republic of Korea
E-mail: leesw@ewha.ac.kr

D. H. Lee, S. Kim, H. Kim, S. Jung
Interdisciplinary Materials Measurement Institute
Korea Research Institute of Standards and Science
Daejeon 34113, Republic of Korea
E-mail: syjung@kriss.re.kr

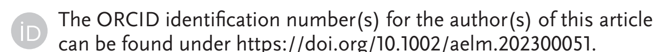
The ORCID identification number(s) for the author(s) of this article can be found under https://doi.org/10.1002/aelm.202300051.

© 2023 The Authors. Advanced Electronic Materials published by Wiley-VCH GmbH. This is an open access article under the terms of the Creative Commons Attribution License, which permits use, distribution and reproduction in any medium, provided the original work is properly cited.

[+]Present address: Department of Precision and Microsystems Engineering, Delft University of Technology, Mekelweg 2 2628 CD Delft, The Netherlands

DOI: 10.1002/aelm.202300051

S.-J. Choi
Institute for Theoretical Physics and Astrophysics
University of Wűrzburg
D-97074 Wűrzburg, Germany

S. Kim
Department of Physics and Astronomy
Sejong University
Seoul 05006, Republic of Korea

K. Watanabe, T. Taniguchi
Advanced Materials Laboratory
National Institute for Materials Science
Tsukuba 305-0044, Japan

E. E. B. Campbell
School of Chemistry
University of Edinburgh
Edinburgh EH9 3FJ, United Kingdom

ADVANCED ELECTRONIC MATERIALS
Open Access
www.advelectronicmat.de

2199160x, 2023, 6, Downloaded from https://onlinelibrary.wiley.com/doi/10.1002/aelm.202300051 by Welsh Assembly Government, Wiley Online Library on [21/07/2023]. See the Terms and Conditions (https://onlinelibrary.wiley.com/terms-and-conditions) on Wiley Online Library for rules of use; OA articles are governed by the applicable Creative Commons License

vdW-assembled heterostructures have also been utilized as effective material metrology platforms to characterize low-dimensional material properties such as the fundamental electronic band structures and electron interactions with various quasiparticles like phonons and magnons.[19–24] The majority of device applications explored to date rely on low-energy direct quantum tunneling; namely, out-of-plane vertical charge flow around the Fermi levels of the vertical heterostacks.[19–27]

It is well established that, as tunnel-electron energies increase at the tunnel junctions, high-energy quantum tunneling events such as Fowler–Nordheim (FN) tunneling or the thermally assisted Schottky emission mechanism play more dominant roles in the quantum charge flow.[24,28,29] FN tunneling, where charges tunnel into the conduction or valence band of tunnel barriers, is distinguished from low-energy direct tunneling that directly drives charge carriers to tunnel into the empty energy states of contact electrodes. FN tunneling has been widely implemented in various conventional electronic and optical device applications, e.g., flash memories, high-resolution electron microscopy, and field-emission displays, to name a few.[30–33] Moreover, since the energy distribution of the FN tunnel charge is much narrower than those of Schottky and thermionic emissions, FN tunneling has considerable potential as a material metrology probe. In particular, the interfaces of vdW-assembled 2D–2D planar junctions are ideal device platforms for validating the conceptual FN tunneling model that considers an atomically flat and clean metal–insulator interface.[34] Additionally, interesting questions arise about whether high-energy FN tunneling, which requires a transformation of the shape of the tunnel barrier, could be realized with single-atomic-layer insulators. Even with these intriguing questions and opportunities, however, experimental realizations of "high-energy" FN tunneling and device applications have been minimal for 2D vdW heterostructures to date.[32,33,35,36] In this report, we demonstrate that FN tunnel driven out-of-plane vertical charge flows are realized in 2D–2D vdW vertical tunnel junctions, which are assembled with ultrathin tunnel barriers down to monolayers of semiconducting transition metal dichalcogenides (SCTMDs). At low temperature, the high electric field-driven FN tunneling displays a layer-by-layer quantum tunneling process that identifies the Fermi level location of the 2D SCTMDs with respect to the conduction or the valence band of each layer. Confinement of electron or hole wave packets in the 2D–2D planar tunnel junctions reduces the vertical charge flow significantly, which relates to a greatly enhanced out-of-plane effective charge carrier mass in the sub-nm thick tunnel insulators.

2. Results and Discussion

2.1. Fowler–Nordheim Tunneling in Monolayer SCTMDs

Figure 1a,b respectively show an optical microscope image and a simplified device schematic of the 2D–2D vdW heterostructures (details of Experimental Section in the Supporting Information). Thin graphite flakes (≥ 5 nm) with clean vdW contacts to the SCTMDs are essential to preserve the intrinsic electrical properties of the tunnel barriers, even down to monolayer thickness.[21–23] Thanks to negligible charge transfer between the graphite electrodes and the SCTMDs,[20,21] the tunnel barrier at the graphite–SCTMD interface, quantified by the Schottky barrier height (Φ_{SB}), is determined by the fundamental SCTMD material properties, namely the relative

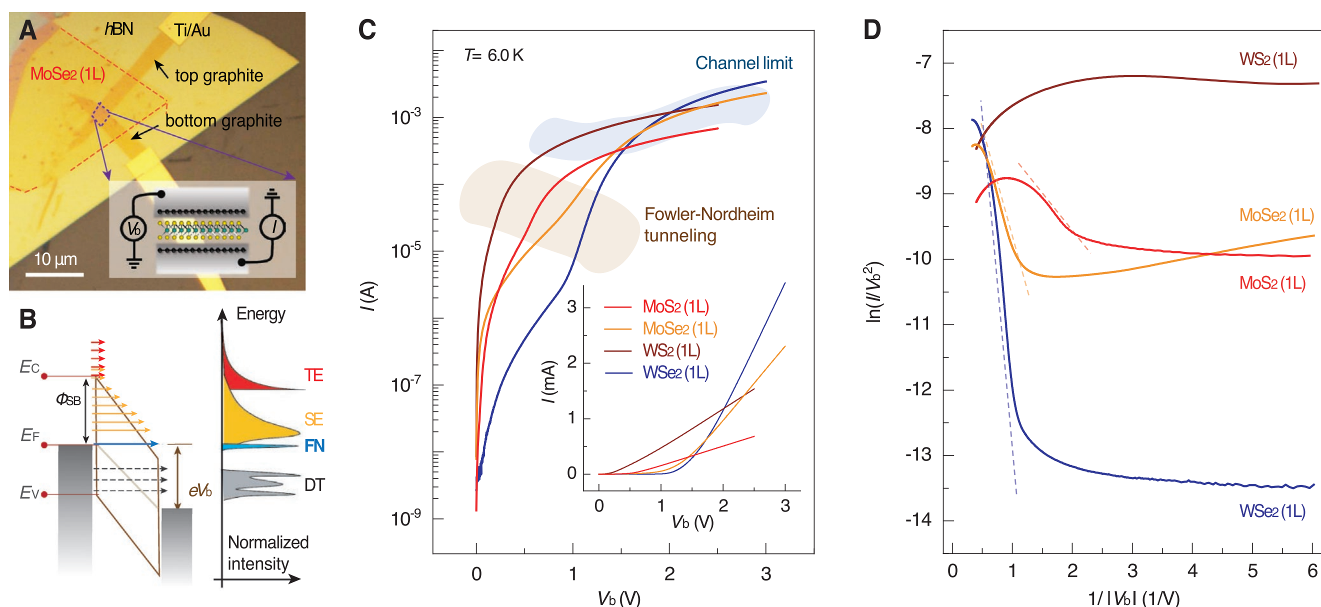

Figure 1. Out-of-plane quantum tunneling processes of van der Waals vertical heterostructures. A) Optical microscope image and a simplified device schematic (inset) of vertical graphite–$MoSe_2$(1L)–graphite planar tunnel junctions. B) Schematic of various tunneling mechanisms and their energy distributions as a function of sample bias voltage (V_b) for electron tunneling. Vertical charge flows are driven by direct tunneling (DT, dashed black lines), FN tunneling (solid blue line), Schottky emission (SE, solid orange lines), and thermionic emission (TE, solid red lines). C) I–V_b characteristic responses, with the I plotted in a logarithm scale and a linear scale (inset). D) $\ln(I/V_b^2)$–$1/V_b$ relations from devices with monolayers of MoS_2, $MoSe_2$, WS_2, and WSe_2 at $T = 6.0$ K. The colored dotted lines indicate the V_b regions where FN tunneling is the main contributor to vertical quantum tunneling, as the linear progression of the FN tunneling plot shows that it dominates charge transport.

© 2023 The Authors. Advanced Electronic Materials published by Wiley-VCH GmbH

positions of the conduction (E_C) or valence (E_V) band edge with respect to the Fermi level (E_F) of the electrode: $\Phi_{SB} = E_C - E_F$ for *n*-type and $\Phi_{SB} = E_F - E_V$ for *p*-type SCTMD films. Figure 1b also illustrates a series of tunneling processes as a sample bias voltage (V_b) sequentially drives the charge flow in the regimes of direct tunneling (dashed black lines), FN tunneling (solid blue line), Schottky emission (SE, solid orange lines), and thermionic emission (TE, solid red lines).[24,28,29] Due to the distinctive path of each tunneling process, V_b-dependent tunnel events reveal specific properties of the tunnel junctions. For instance, high-energy tunneling such as FN, SE, and TE is sensitive to the electronic structure of the tunnel barrier material, whereas low-energy direct tunneling is subject to the barrier's mid-gap states between E_C and E_V. Since FN tunneling occurs only near the E_F of the source electrode at low temperature, moreover, the electron energy distributions corresponding to FN tunneling become very narrow. Consequently, as illustrated in Figure 1b, FN tunnel driven charges are confined to an energy window around the E_C (or E_V) edge, underlining the potential for a practical material metrology probe utilizing high-energy FN tunneling.

A collection of I–V_b characteristic curves at $T = 6.0$ K is displayed in Figure 1c for vertical tunnel junctions with monolayer MoS_2, $MoSe_2$, WS_2, and WSe_2 tunnel barriers. The I–V_b characteristics exhibit a clear nonlinearity as a function of V_b (Figure 1c inset), indicating that the transport of charge carriers through the monolayer SCTMD is governed by quantum mechanical tunneling processes. At low temperatures where thermally activated Schottky emission becomes effectively suppressed, a series of quantum transport processes of direct tunneling, FN tunneling, and channel-limited ohmic conduction sequentially dominate the quantum transport through the junctions. As illustrated in Figure 1b, FN tunneling initiates when the lowered (raised) Fermi level of the biased electrode (the right one in Figure 1b) aligns with the valence (conduction) band edge of the tunnel barrier at $-eV_b$ (eV_b), accompanied by a transformation of the tunnel barrier shape from trapezoidal to triangular. The FN tunnel driven current can be expressed as

$$I = \frac{Ae^3 m_e V_b^2}{8\pi h m^* d^2 \Phi_{SB}} \exp\left(\frac{-8\pi d\left(2m^*\right)^{\frac{1}{2}}}{3ehV_b}\Phi_{SB}^{\frac{3}{2}}\right) \tag{1}$$

where A, h, d, m_e, and m^* respectively indicate the tunnel junction area, Planck's constant, tunnel barrier width, free electron mass, and effective mass of the tunneling charge carrier.[28,37]

The linear progressions in the FN tunnel relation of $\ln(I/V_b^2)$ versus $1/V_b$ at high V_b, as marked with dotted lines in Figure 1d indicate that the vertical charge flows are primarily driven by FN tunneling, even in the devices with a $d \approx 0.6$ nm thick monolayer SCTMD. However, when comparing different monolayers, $MoSe_2$ and WSe_2 clearly show a linear behavior when $1/V_b$ is less than ca. 1 V^{-1}. Note that the voltages at which FN tunneling starts to develop are lower for the S-based SCTMDs than for their Se-based counterparts, indicating that Φ_{SB} is lower in the devices with WS_2 and MoS_2 than in those with $MoSe_2$ and WSe_2. Our previous report showed that sulfur atom vacancies and the resultant mid-gap states, likely leading to the Φ_{SB} reductions in the MoS_2 and WS_2 devices, are conspicuous in the S-based monolayer SCTMD films.[20] The lowered tunnel barrier heights and the substantial leakage current through the mid-gap states allow a large amount of low-energy charge carriers to flow, even before high-energy FN tunneling becomes effective. In comparison, WSe_2 and $MoSe_2$ films are less prone to form selenium atom vacancies, so that the high-energy FN tunnel features can clearly appear in the tunnel junctions with monolayer WSe_2 and $MoSe_2$ where there is a larger Φ_{SB} and a reduced leakage current.

2.2. Fowler–Nordheim Tunneling as a Material Characterization Probe

High-energy FN tunnel characteristic measurements can address a couple of critical 2D SCTMD material properties. To accurately assess V_{FN}, we replot the data as the numerical derivative, $d(\ln(I/V_b^2))/d(1/V_b)$ versus V_b, to accentuate the evolution of the FN plot slope upon changing V_b. The FN plot slope, defined as $-8\pi d(2m^*\Phi_{SB}^3)^{\frac{1}{2}}/3eh$, is determined by three independent junction parameters: d, m^*, and Φ_{SB}. A considerable negative value of the gradient of the FN plots indicates that the FN tunnel driven charges effectively feel more resistance and the current is moderated due to either a heavier m^*, a higher Φ_{SB}, or a thicker d. In that regard, we can refer the magnitude of the FN plot derivative, $|d(\ln(I/V_b^2))/d(1/V_b)|$, to an effective FN tunnel junction resistance at a specific V_b. **Figure 2** displays a series of FN plot derivative curves for graphite–WSe_2–graphite junctions with mono-, bi-, and tri-layer WSe_2. The FN plot derivative curves, shown with solid blue lines in Figure 2, are obtained by numerically averaging as many as 61 individual plots (gray dots in Figure 2), some of which represent data with different gate voltages applied to the $Si/SiO_2/h$BN back gate. Note that the V_b at which the FN tunnel junction resistance reaches its first local maximum (first minimum on the derivative plot), indicated with vertical orange arrows in Figure 2, consistently decreases as the WSe_2 layer number increases.

We associate V_{FN} with the sample bias where the FN plot derivative reaches its first minimum and accordingly assign Φ_{SB} of the junction as eV_{FN}. As the V_b increases beyond V_{FN}, the tunnel junction resistance quickly switches from a higher to a lower resistance state, reflecting a direct transformation of the tunnel barrier from a trapezoid with a fixed d to a triangle with a shortening d. Since the FN tunnel junction resistance lowers its value as V_b progressively increases, we can relate the first local FN tunnel plot derivative minimum to the point where FN tunneling starts to dominate. Similarly, the last minimum in the derivative curve is interpreted as the transition point from FN tunneling to channel-limited ohmic conduction. Thus, the region between the first and last minima represents the domain in which FN tunneling governs the charge transport. In Figure 2a, the monolayer WSe_2 junction displays two minima in the derivative curve, confirming the occurrence of FN tunneling in this area. The vertical orange arrows in Figure 2 indicate V_{FN} for each device, and the corresponding Schottky barrier heights are 1.23 eV (Figure 2a), 1.03 eV (Figure 2b), and 0.93 eV (Figure 2c) for mono-, bi-, and tri-layer

© 2023 The Authors. Advanced Electronic Materials published by Wiley-VCH GmbH

2199160x, 2023, 6, Downloaded from https://onlinelibrary.wiley.com/doi/10.1002/aelm.202300051 by Welsh Assembly Government, Wiley Online Library on [21/07/2023]. See the Terms and Conditions (https://onlinelibrary.wiley.com/terms-and-conditions) on Wiley Online Library for rules of use; OA articles are governed by the applicable Creative Commons License

ADVANCED ELECTRONIC MATERIALS
Open Access
www.advelectronicmat.de

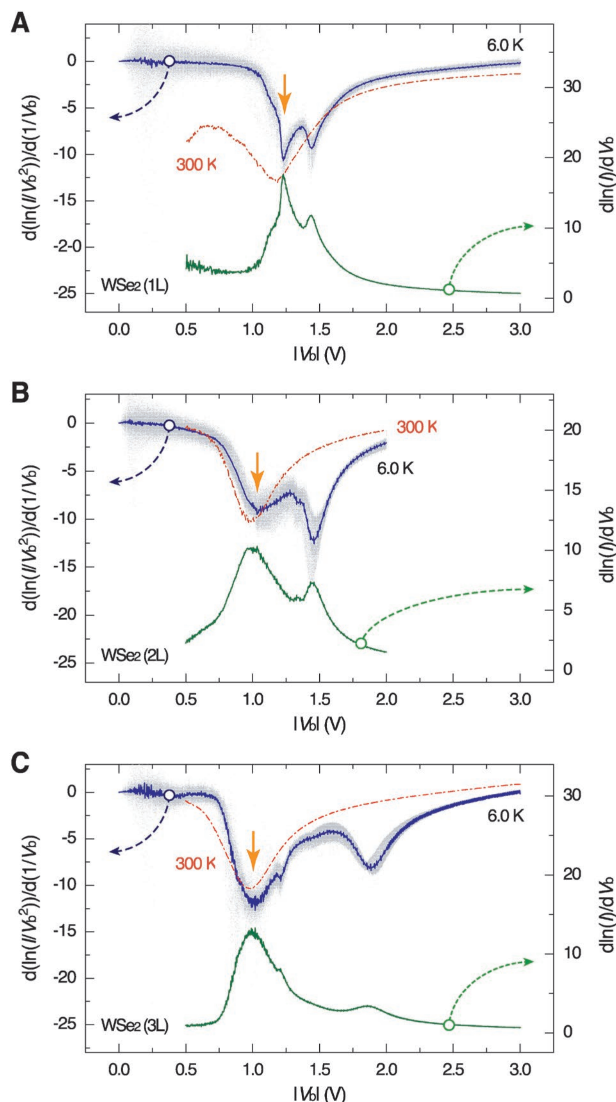

Figure 2. FN plot analyses of WSe_2 vertical tunnel junctions. Layer-number-dependent FN plot derivative curves calculated from the I–V_b characteristic responses at T = 6.0 K (solid blue lines) and T = 300 K (dotted red lines) from graphite–WSe_2–graphite vertical junctions with A) mono-, B) bi-, and C) tri-layer WSe_2 as a tunnel insulator. Orange arrows indicate the first FN tunnel plot derivative dip at the V_{FN} that can be assigned to the Schottky barrier height $\Phi_{SB} = eV_{FN}$. The solid green lines indicate $\mathrm{dln}(I)/\mathrm{d}V_b$ versus V_b relations at T = 6.0 K, revealing similar V_b-dependent spectral features as those from the FN plot derivative relations.

WSe_2 junctions, respectively. We attribute the observed layer-number-dependent Φ_{SB} reduction to the energy gap shrinkage in multilayer WSe_2.[38] With the estimated Φ_{SB}, the lower boundaries of the WSe_2 quasiparticle energy gaps (E_G) can be determined to be $E_G \geq 2\Phi_{SB}$. For example, the estimated energy gap of the monolayer WSe_2, E_G (1L-WSe_2) ≥ 2.4 eV, agrees well with previous reports, suggesting that the Fermi level of WSe_2 is located in the middle of the energy gap or marginally shifted toward the valence band edge.[20,38] The red dotted lines in Figure 2 indicate the FN tunnel plot derivative curves at T = 300 K for each tunnel junction. A single minimum in the FN plot derivative forms at a bias voltage that is slightly lower than V_{FN} at T = 6.0 K, reflecting the narrowing energy gaps of the semiconducting films upon elevating the temperature.[20,39] Our approach to analyzing Φ_{SB} based on the FN plot slopes can be further corroborated with the theoretical model proposed by K. H. Gundlach: the energy barriers in metal–insulator–metal tunnel junctions can be related to the peak positions in $\mathrm{dln}(I)/\mathrm{d}V_b$ versus V_b plots.[40,41] The solid green lines in Figure 2b,c display the $\mathrm{dln}(I)/\mathrm{d}V_b$–$V_b$ relations for each WSe_2 tunnel junction, with the first peak aligned well with V_{FN}. **Figure 3**a–d summarize the layer-number-dependent Φ_{SB} of the WSe_2, $MoSe_2$, WS_2, and MoS_2 tunnel devices, respectively. Diminishing Φ_{SB} with increasing layer number is consistent across the type-VI SCTMDs. Note that Φ_{SB} of the devices with MoS_2 films are consistently lower than the heights for other junctions, and also Φ_{SB} for the monolayer WS_2 device is severely underestimated since FN tunneling was not fully developed for these measurements (Figure 1d).

2.3. Redefinition of Vertical Effective Mass in Ultrathin SCTMDs

Φ_{SB} can be determined from the location of V_{FN} in the FN tunnel resistance plots and d by measuring the SCTMD thickness with an atomic force microscope. Therefore, it is possible to extract the charge carrier effective masses in the SCTMD vertical junctions from the measured gradients. As displayed in **Figure 4**, the extracted carrier effective masses are found to be much larger than the free electron mass in the monolayer devices, $m^*(\text{1L-WSe}_2)/m_e \cong 3$. As the WSe_2 layer number increases, the effective mass decreases and converges to $m^*/m_e \cong 0.2$–0.3. The convergence for high layer numbers to a value of ca. $0.2m_e$ for WSe_2 is in reasonable agreement with earlier measurements for thick WSe_2 layers (> 10 nm).[36] WSe_2 at 300 K and $MoSe_2$ at 6 K show a similar dependency of effective carrier mass on layer number (Figures S2 and S3, Supporting Information).

The increased charge carrier effective masses for low layer numbers reflect the unique quantum tunneling processes in vdW-coupled planar 2D–2D junctions with an ultrathin tunnel insulator. In 2D vdW materials, the energy-momentum relations along the z-axis cannot be explicitly defined because of the weak interlayer coupling. Thus, the "effective" masses extracted from the out-of-plane FN tunneling should differ from both the effective masses obtained for 3D bulk materials and the in-plane 2D carrier effective masses. Considering the energy-time uncertainty principle $\Delta E \Delta t \sim \hbar/2$, we can argue that charge carriers tunneling through the 2D barrier momentarily stay in the tunnel junction for $\Delta t \sim \hbar/(2\Delta E)$, which is related to the resonant tunnel lifetime in a semiconductor tunnel junction where ΔE is the half-width half-maximum of the transmission coefficient.[42] During this transitory stay, charges travel by $\lambda = v\Delta t$, later expressed as $\lambda = \hbar/(2m^*\Delta E)^{1/2}$ by combining the de Broglie wave $p = m^*v = \hbar/\lambda$ and the uncertainty principle for Δt; namely, a lighter effective mass indicates that tunneling charges can transport deeper into the barriers. For the particular case that the thickness of an insulating layer d becomes thinner than λ, the penetration depth λ can naturally be replaced by d. Following this simple heuristic argument, we

© 2023 The Authors. Advanced Electronic Materials published by Wiley-VCH GmbH

2199160x, 2023, 6, Downloaded from https://onlinelibrary.wiley.com/doi/10.1002/aelm.202300051 by Welsh Assembly Government, Wiley Online Library on [21/07/2023]. See the Terms and Conditions (https://onlinelibrary.wiley.com/terms-and-conditions) on Wiley Online Library for rules of use; OA articles are governed by the applicable Creative Commons License

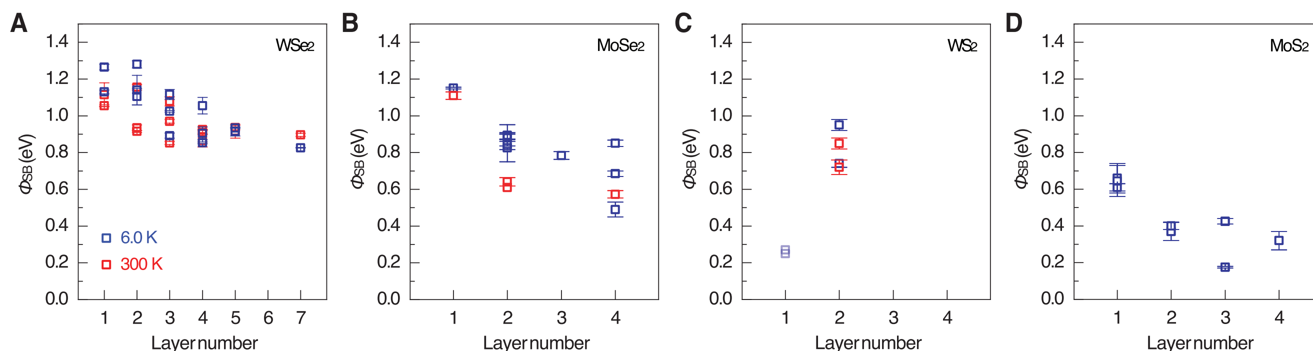

Figure 3. Layer-number-dependent Schottky barrier heights. Schottky barrier height variations in the 2D semiconducting layers of A) WSe_2, B) $MoSe_2$, C) WS_2, and D) MoS_2. The blue and red open squares represent Φ_{SB} extracted from the high-energy FN tunnel characteristics at $T = 6.0$ K and $T = 300$ K. We extract two values of the barrier heights from the I–V_b characteristic measurements for positive and negative V_b; the open squares and solid lines represent their mean and difference.

can make two postulates: i) the bulk effective mass m^* defines the critical thickness $d_c = \hbar/(2m^*\Delta E)^{1/2}$ at which the vertical quantum tunneling exhibits a crossover from bulk to 2D multiband transport, and ii) the "equivalent" charge carrier effective mass in an atomically thin SCTMD insulator reconfigures as $m^*_{2D} = \hbar^2/(2\Delta E d^2)$.

Figure 4 compares the experimentally extracted masses with the theoretically deduced "equivalent" effective mass variations. We consider ΔE for WSe_2 layers as 0.6 eV and the thickness of monolayer WSe_2 as 0.65 nm. ΔE is determined to be half of the voltage range, 0.8–2.0 V, where FN tunneling behavior is observed from the 2L, 3L, and 4L WSe_2 in Figure 2,5. With the bulk effective mass set as $m^* = 0.25m_e$, d_c is estimated to be 1.79 nm, and thus the crossover between bulk and multiband 2D SCTMDs is expected to occur at three layers of WSe_2. The

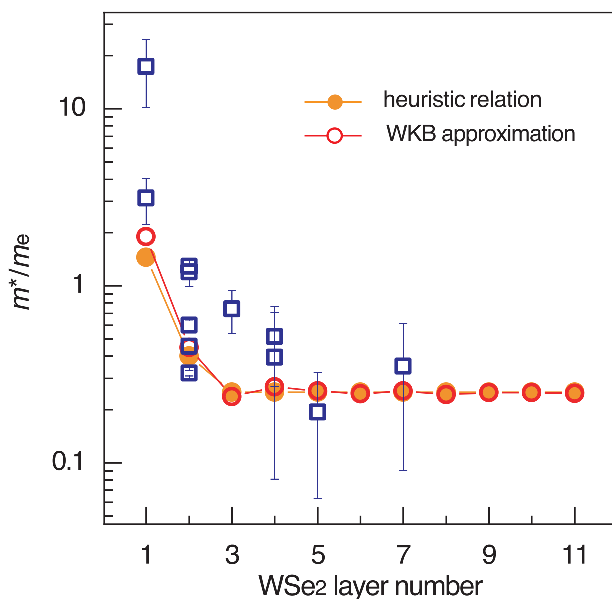

Figure 4. Layer-number-dependent effective mass. Layer-number-dependent vertical effective mass distributions probed by the high-energy FN tunnel analyses of graphite–WSe_2–graphite vertical tunnel junctions. Closed orange and open red circles respectively indicate the effective mass variations estimated from the simple heuristic model and quantum transport simulations.

effective mass variations derived from simulated I–V_b characteristic responses incorporating microscopic out-of-plane quantum tunneling processes (open red circles in Figure 4) are well matched to the experimental data and the simple heuristic model calculation (more details in the Supporting Information).

2.4. Sequential Layer-by-layer Fowler–Nordheim Quantum Tunneling

We argue that a sequential layer-by-layer FN tunneling process regulates the high-energy out-of-plane charge flow, and also that the FN tunneling measurements presented here are sensitive enough to probe the microscopic quantum tunneling events in the 2D vdW semiconducting layers. We find that graphite–SCTMD–graphite vertical tunnel junctions, particularly the devices with WSe_2 and $MoSe_2$, reveal fine spectral features in a layer-number-specific manner other than the leading derivative dip at V_{FN} in the FN plot derivative curves. **Figure 5**a shows the FN plot derivative for a 4L-WSe_2 junction at $T = 6.0$ K. When V_b increases beyond V_{FN} (0.88 V), several additional features appear for the V_b range up to 2 V: specifically, four additional distinct minima can be discerned in the FN plot derivative curve, indicated by the gray arrows in Figure 5a. Similar spectral features are also found in other WSe_2 devices, as shown in Figure 2.

The schematic illustrations in Figure 5b–f display the successive microscopic layer-by-layer tunneling process in p-type 4L-WSe_2 devices. In tunnel junctions with 3D bulk materials, charge carriers that have tunneled through the barrier need to transport through the tunnel insulator's conduction (or valence) band before draining out to a contact electrode. However, for ideal 2D SCTMD tunnel devices at low temperature, the high-energy FN tunnel driven charges successively access the individual layers of the SCTMD as the sample bias progressively increases. First, E_F of the graphite source becomes aligned with E_V of the bottom-most WSe_2 layer (i.e., next to the drain electrode) at $V_b = V_{FN}$ (Figure 5c), initiating FN tunneling. As V_b continuously increases and tunnel charges fill the bottom-most WSe_2 layer, E_F of the graphite source remains fixed to E_V of this layer. At the same time, the increasing electric field keeps tilting the triangular-shaped tunnel barrier and lowering the

© 2023 The Authors. Advanced Electronic Materials published by Wiley-VCH GmbH

2199160x, 2023, 6, Downloaded from https://onlinelibrary.wiley.com/doi/10.1002/aelm.202300051 by Welsh Assembly Government, Wiley Online Library on [21/07/2023]. See the Terms and Conditions (https://onlinelibrary.wiley.com/terms-and-conditions) on Wiley Online Library for rules of use; OA articles are governed by the applicable Creative Commons License

ADVANCED ELECTRONIC MATERIALS
Open Access
www.advelectronicmat.de

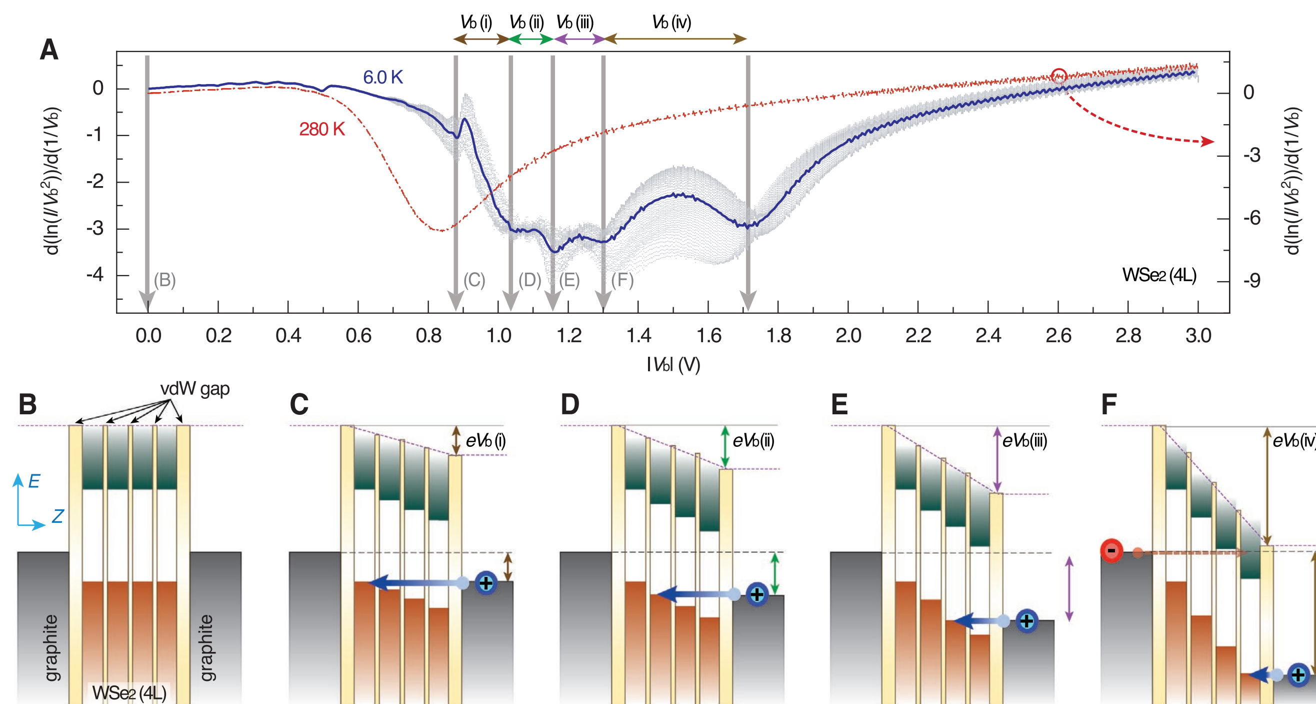

Figure 5. Sequential layer-by-layer FN tunneling process. A) FN plot derivative relation of the tetra-layer WSe_2(4L) tunnel junction at $T = 6.0$ K (blue line) and 280 K (dotted red line). Vertical gray arrows respectively indicate the V_b regions of V_b(i), V_b(ii), V_b(iii), and V_b(iv) for the layer-by-layer FN tunneling process. B–F) Schematic illustrations of the band alignments of the graphite–WSe_2(4L)–graphite 2D–2D vdW vertical tunnel junctions in the initial state $V_b = 0$ V B), V_b(i) C), V_b(ii) D), V_b(iii) E), and V_b(iv) F).

FN tunnel junction resistance. As the tunneling charges continue to enter the bottom-most WSe_2 layer, the energy cost for electrons to fill this individual WSe_2 layer is also built up. The augmented charging energies finally lead to an increase in the FN tunnel junction resistance. The switchover from a low to a high FN tunnel junction resistance develops a spectral peak (or bump) in the FN plot derivative curve. Next, the Fermi level of the second layer (from the bottom) is pulled down to the Fermi level of the graphite source once the first (or bottom-most) layer is filled, after which FN tunneling to the second WSe_2 layer starts (Figure 5d), producing a second minimum in the FN tunnel junction resistance plot. In the following V_b range of $1.0 \text{ V} \leq V_b \leq 1.2$ V, tunneling holes fill the second WSe_2 layer, and subsequent FN tunnel junction resistance variations lead to the second FN plot derivative bump. Accordingly, we can associate the third and fourth FN plot derivative peaks with the tunneling hole carriers filling the third and top-most WSe_2 layers. When the last WSe_2 layer is completely filled, the vertical charge flows are limited by the ohmic conduction of the graphite electrodes.

3. Conclusion

We investigate the microscopic quantum transport processes of out-of-plane vertical charge flows in atomically thin 2D vdW SCTMD layers, especially in the "high-energy" FN tunneling regime. The high electric field-driven vertical charge flows can be utilized as a reliable material characterization probe to quantitatively address the relative Fermi level locations of the SCTMDs and the layer numbers of WSe_2 and $MoSe_2$. Detailed FN plot analyses indicate that out-of-plane charge flows are regulated by sequential tunneling, involving all layers of the SCTMD tunnel barriers successively. Moreover, electron and hole carriers tunneling across the 2D–2D planar junctions are held by momentary confinements in the ultrathin tunnel barriers, which materializes as enhanced out-of-plane charge carrier effective masses in the FN tunnel relations. The high-energy FN tunneling realized in our studies can provide a solid experimental foundation for understanding vertical charge flows in 2D semiconductors, and thus promote FN tunnel device applications with vdW-assembled vertical heterostructures.

4. Experimental Section

Device Fabrication: In vertical 2D vdW heterostructures, the preparation of atomically clean interfaces was critical for an accurate and reliable material characterization of the vertical junctions. At first, 60 nm to 100 nm thick highly crystalline *h*BN flakes were mechanically exfoliated on a 90 nm thick SiO_2 layer on Si substrate. Then a mechanically isolated graphite flake of thickness 5 nm or more was transferred to a pre-located *h*BN flake on the SiO_2/Si substrate using a dry transfer method. Polymer stacks of PMMA (poly (methyl methacrylate))–PSS (polystyrene sulfonate) layers was utilized for such tasks and carefully adjust the thickness of each layer to enhance the optical contrast of the exfoliated ultrathin 2D layered materials. The PMMA film in warm (60 °C) acetone was removed and further anneal the samples at 350 °C for several hours in a mixture of Ar:H_2 = 9:1 to ensure residue-free graphite surfaces. Then by following a similar dry transfer protocol, SCTMD films were transferred on top of the pre-located Si/SiO_2/*h*BN/graphite stack. In removing the polymer, the temperature to 250°C was reduced

© 2023 The Authors. Advanced Electronic Materials published by Wiley-VCH GmbH

2199160x, 2023, 6, Downloaded from https://onlinelibrary.wiley.com/doi/10.1002/aelm.202300051 by Welsh Assembly Government, Wiley Online Library on [21/07/2023]. See the Terms and Conditions (https://onlinelibrary.wiley.com/terms-and-conditions) on Wiley Online Library for rules of use; OA articles are governed by the applicable Creative Commons License

to avoid undesired defect state formation in the SCTMDs. In some devices, instead of using the PSS/PMMA polymer stacks, a Gel-Pak was utilized to exfoliate and transfer SCTMDs to form SCTMD–graphite vertical junctions. Lastly, a top graphite flake exfoliated on a PMMA–PSS polymer stack was transferred to complete the vertical graphite–SCTMD–graphite planar tunnel junctions. The tunnel devices through electron-beam lithography and metal lift-off (Ti ≈ 5 nm/Au ≈ 80 nm) was completed. High-purity (> 99.995%) SCTMD crystals of WSe_2, $MoSe_2$, WS_2, and MoS_2 from HQ Graphene were purchased with no additional dopants added during the growth procedure.

I–Vb characteristic Measurements: The I–V_b characteristic measurements were carried out by sweeping a bias voltage V_b at a specific gate voltage V_g using a DC voltage source (Yokogawa GS200). The current was converted into voltage using a low-noise voltage preamplifier (Digital Instruments DL1211) and then recorded using a digital multimeter (Agilent 34410A). The gate voltage was varied over a range of $V_g = -30$ V to 30 V, with an increment of $\Delta V_g = 1$ V. The measurements were conducted at temperatures of 6.0 and 300 K, at the minimum pressures of 10^{-7} Torr and 2×10^{-3} Torr.

Supporting Information

Supporting Information is available from the Wiley Online Library or from the author.

Acknowledgements

D.H.S., D.-H.L., and S.-J.C. contributed equally to this work. The authors thank T.-Y. Jeong, G. Min, and H. Kim for their support in device fabrications and measurements. The authors also thank D.-H. Ha for his help in Raman spectroscopy measurements for SCTMD layer-number identification. This work was supported by Basic Science Research Programs (NRF-2017R1D1A1B03035727, 2019R1A2C2004007, 2021R1A6A1A10039823, 2022R1A2B5B01001640 and 2022R1A2C2008140) and Global Research and Development Center Program (2018K1A4A3A01064272) through the National Research Foundation of Korea. This work was also supported by Human Frontier Science Program (RGP00026/2019), the Würzburg-Dresden Cluster of Excellence on Complexity and Topology in Quantum Matter (EXC2147, project-id 390858490) and by the DFG (SPP1666 and SFB1170 "ToCoTronics").

Conflict of Interest

The authors declare no conflict of interest.

Data Availability Statement

The data that support the findings of this study are available from the corresponding author upon reasonable request.

Keywords

2D semiconductors, electron and hole field emission, Fowler-Nordheim tunneling, Schottky-barrier height, van der Waals vertical heterostructures

Received: January 27, 2023
Revised: March 7, 2023
Published online: April 14, 2023

[1] Y. Liu, J. Guo, E. Zhu, L. Liao, S. J. Lee, M. Ding, I. Shakir, V. Gambin, Y. Huang, X. Duan, *Nature* **2018**, *557*, 696.
[2] X. Yu, P. Yu, D. Wu, B. Singh, Q. Zeng, H. Lin, W. Zhou, J. Lin, K. Suenaga, Z. Liu, Q. J. Wang, *Nat. Commun.* **2018**, *9*, 1545.
[3] T. Georgiou, R. Jalil, B. D. Belle, L. Britnell, R. V. Gorbachev, S. V. Morozov, Y. J. Kim, A. Gholinia, S. J. Haigh, O. Makarovsky, L. Eaves, L. A. Ponomarenko, A. K. Geim, K. S. Novoselov, A. Mishchenko, *Nat. Nanotechnol.* **2013**, *8*, 100.
[4] W. J. Yu, Z. Li, H. Zhou, Y. Chen, Y. Wang, Y. Huang, X. Duan, *Nat. Mater.* **2013**, *12*, 246.
[5] A. Li, Q. Chen, P. Wang, Y. Gan, T. Qi, P. Wang, F. Tang, J. Z. Wu, R. Chen, L. Zhang, Y. Gong, *Adv. Mater.* **2019**, *31*, 1805656.
[6] X. Zhang, B. Liu, L. Gao, H. Yu, X. Liu, J. Du, J. Xiao, Y. Liu, L. Gu, Q. Liao, Z. Kang, Z. Zhang, Y. Zhang, *Nat. Commun.* **2021**, *12*, 1522.
[7] A. Mishchenko, J. S. Tu, Y. Cao, R. V. Gorbachev, J. R. Wallbank, M. T. Greenaway, V. E. Morozov, S. V. Morozov, M. J. Zhu, S. L. Wong, F. Withers, C. R. Woods, Y. J. Kim, K. Watanabe, T. Taniguchi, E. E. Vdovin, O. Makarovsky, T. M. Fromhold, V. I. Fal'ko, A. K. Geim, L. Eaves, K. S. Novoselov, *Nat. Nanotechnol.* **2014**, *9*, 808.
[8] Y. C. Lin, R. K. Ghosh, R. Addou, N. Lu, S. M. Eichfeld, H. Zhu, M. Y. Li, X. Peng, M. J. Kim, L. J. Li, R. M. Wallace, S. Datta, J. A. Robinson, *Nat. Commun.* **2015**, *6*, 7311.
[9] A. Di Bartolomeo, F. Urban, M. Passacantando, N. McEvoy, L. Peters, L. Iemmo, G. Luongo, F. Romeo, F. Giubileo, *Nanoscale* **2019**, *11*, 1538.
[10] L. Tong, Z. Peng, R. Lin, Z. Li, Y. Wang, X. Huang, K.-H. Xue, H. Xu, F. Liu, H. Xia, P. Wang, M. Xu, W. Xiong, W. Hu, J. Xu, X. Zhang, L. Ye, X. Miao, *Science* **2021**, *373*, 1353.
[11] A. Pelella, A. Grillo, F. Urban, F. Giubileo, M. Passacantando, E. Pollmann, S. Sleziona, M. Schleberger, A. Di Bartolomeo, *Adv. Electron. Mater.* **2021**, *7*, 2000838.
[12] X. X. Li, Z. Q. Fan, P. Z. Liu, M. L. Chen, X. Liu, C. K. Jia, D. M. Sun, X. W. Jiang, Z. Han, V. Bouchiat, J. J. Guo, J. H. Chen, Z. D. Zhang, *Nat. Commun.* **2017**, *8*, 970.
[13] M. S. Choi, G. H. Lee, Y. J. Yu, D. Y. Lee, S. H. Lee, P. Kim, J. Hone, W. J. Yoo, *Nat. Commun.* **2013**, *4*, 1624.
[14] C. Liu, X. Yan, X. Song, S. Ding, D. W. Zhang, P. Zhou, *Nat. Nanotechnol.* **2018**, *13*, 404.
[15] C. H. Liu, G. Clark, T. Fryett, S. Wu, J. Zheng, F. Hatami, X. Xu, A. Majumdar, *Nano Lett.* **2017**, *17*, 200.
[16] F. Withers, O. Del Pozo-Zamudio, A. Mishchenko, A. P. Rooney, A. Gholinia, K. Watanabe, T. Taniguchi, S. J. Haigh, A. K. Geim, A. I. Tartakovskii, K. S. Novoselov, *Nat. Mater.* **2015**, *14*, 301.
[17] M. Long, E. Liu, P. Wang, A. Gao, H. Xia, W. Luo, B. Wang, J. Zeng, Y. Fu, K. Xu, W. Zhou, Y. Lv, S. Yao, M. Lu, Y. Chen, Z. Ni, Y. You, X. Zhang, S. Qin, Y. Shi, W. Hu, D. Xing, F. Miao, *Nano Lett.* **2016**, *16*, 2254.
[18] P. Wang, S. Liu, W. Luo, H. Fang, F. Gong, N. Guo, Z. G. Chen, J. Zou, Y. Huang, X. Zhou, J. Wang, X. Chen, W. Lu, F. Xiu, W. Hu, *Adv. Mater.* **2017**, *29*, 1604439.
[19] S. Jung, M. Park, J. Park, T.-Y. Jeong, H.-J. Kim, K. Watanabe, T. Taniguchi, D. H. Ha, C. Hwang, Y.-S. Kim, *Sci. Rep.* **2015**, *5*, 16642.
[20] T. Y. Jeong, H. Kim, S. J. Choi, K. Watanabe, T. Taniguchi, K. J. Yee, Y. S. Kim, S. Jung, *Nat. Commun.* **2019**, *10*, 3825.
[21] D. H. Lee, S. J. Choi, H. Kim, Y.-S. Kim, S. Jung, *Nat. Commun.* **2021**, *12*, 4520.
[22] D. R. Klein, D. MacNeill, J. L. Lado, D. Soriano, E. Navarro-Moratalla, K. Watanabe, T. Taniguchi, S. Manni, P. Canfield, J. Fernández-Rossier, P. Jarillo-Herrero, *Science* **2018**, *360*, 1218.
[23] D. Ghazaryan, M. T. Greenaway, Z. Wang, V. H. Guarochico-Moreira, I. J. Vera-Marun, J. Yin, Y. Liao, S. V. Morozov, O. Kristanovski, A. I. Lichtenstein, M. I. Katsnelson, F. Withers, A. Mishchenko, L. Eaves, A. K. Geim, K. S. Novoselov, A. Misra, *Nat. Electron.* **2018**, *1*, 344.

 © 2023 The Authors. Advanced Electronic Materials published by Wiley-VCH GmbH

2199160x, 2023, 6, Downloaded from https://onlinelibrary.wiley.com/doi/10.1002/aelm.202300051 by Welsh Assembly Government, Wiley Online Library on [21/07/2023]. See the Terms and Conditions (https://onlinelibrary.wiley.com/terms-and-conditions) on Wiley Online Library for rules of use; OA articles are governed by the applicable Creative Commons License

[24] S. Kim, D. H. Shin, Y.-S. Kim, I.-H. Lee, C.-W. Lee, S. Seo, S. Jung, *ACS Appl. Mater. Interfaces* **2021**, *13*, 27705.
[25] S. Jung, N. Myoung, J. Park, T. Y. Jeong, H. Kim, K. Watanabe, T. Taniguchi, D. H. Ha, C. Hwang, H. C. Park, *Nano Lett.* **2017**, *17*, 206.
[26] H. Kim, N. Leconte, B. L. Chittari, K. Watanabe, T. Taniguchi, A. H. MacDonald, J. Jung, S. Jung, *Nano Lett.* **2018**, *18*, 7732.
[27] Z. R. Kudrynskyi, J. Kerfoot, D. Mazumder, M. T. Greenaway, E. E. Vdovin, O. Makarovsky, Z. D. Kovalyuk, L. Eaves, P. H. Beton, A. Patanè, *Commun. Phys.* **2020**, *3*, 16.
[28] F. C. Chiu, *Adv. Mater. Sci. Eng.* **2014**, *2014*, 578168.
[29] G. Nazir, H. Kim, J. Kim, K. S. Kim, D. H. Shin, M. F. Khan, D. S. Lee, J. Y. Hwang, C. Hwang, J. Suh, J. Eom, S. Jung, *Nat. Commun.* **2018**, *9*, 5371.
[30] A. Di Bartolomeo, H. Rücker, P. Schley, A. Fox, S. Lischke, K.-Y. Na, *Solid-State Electron.* **2009**, *53*, 644.
[31] A. A. Talin, K. A. Dean, J. E. Jaskie, *Solid State Electron* **2001**, *45*, 963.
[32] A. Patra, M. A. More, D. J. Late, C. S. Rout, *J. Mater. Chem. C* **2021**, *9*, 11059.
[33] X. Shao, A. Khursheed, *Appl. Sci.* **2018**, *8*, 868.
[34] Y. S. Ang, L. Cao, L. K. Ang, *InfoMat* **2021**, *3*, 502.
[35] L. Liu, C. Liu, L. Jiang, J. Li, Y. Ding, S. Wang, Y.-G. Jiang, Y.-B. Sun, J. Wang, S. Chen, D. W. Zhang, P. Zhou, *Nat. Nanotechnol.* **2021**, *16*, 874.
[36] Y. Zhu, R. Zhou, F. Zhang, J. Appenzeller, *Nanoscale* **2017**, *9*, 19108.
[37] J. G. Simmons, *J. Appl. Phys.* **1963**, *34*, 1793.
[38] D. L. Duong, S. J. Yun, Y. H. Lee, *ACS Nano* **2017**, *11*, 11803.
[39] K. P. O'Donnell, X. Chen, *Appl. Phys. Lett.* **1991**, *58*, 2924.
[40] K. H. Gundlach, *Solid State Electron* **1972**, *15*, 329.
[41] K. H. Gundlach, *J. Appl. Phys.* **1973**, *44*, 5005.
[42] P. Panchadhyayee, R. Biswas, A. Khan, P. K. Mahapatra, *J. Appl. Phys.* **2008**, *104*, 084517.

© 2023 The Authors. Advanced Electronic Materials published by Wiley-VCH GmbH

2199160x, 2023, 6, Downloaded from https://onlinelibrary.wiley.com/doi/10.1002/aelm.202300051 by Welsh Assembly Government, Wiley Online Library on [21/07/2023]. See the Terms and Conditions (https://onlinelibrary.wiley.com/terms-and-conditions) on Wiley Online Library for rules of use; OA articles are governed by the applicable Creative Commons License